The ΔQ-method: State of health and degradation mode estimation for lithium-ion batteries using a mechanistic model with relaxed voltage points

Tobias Hofmann [a,b,*], Jiahao Li [b], Jacob Hamar [b], Simon Erhard [b], Jan Philipp Schmidt [a]

[a] *Chair of Systems Engineering for Electrical Energy Storage, University of Bayreuth, Weiherstraße 26, Bayreuth, 95448, Bavaria, Germany*
[b] *BMW Group, Petuelring 130, Munich, 80809, Bavaria, Germany*

HIGHLIGHTS

- A novel method for full OCV curve reconstruction is introduced.
- Method utilizes captured relaxed voltage points within the last month.
- Method works with only three relaxed voltage points within a SOC window of 30 % to 75 %.
- Method is validated with real-world vehicle data from the BMW i3.

GRAPHICAL ABSTRACT
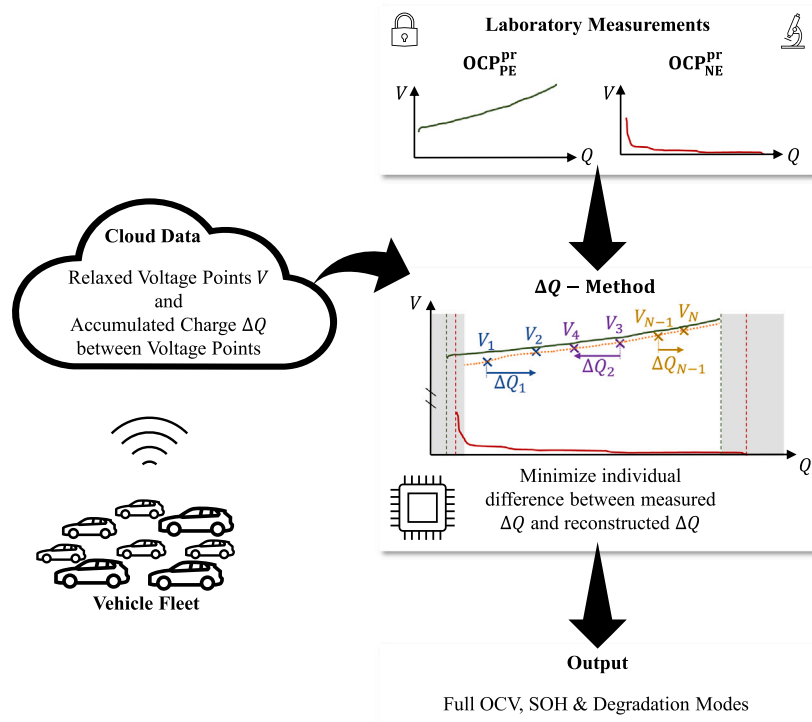
ARTICLE INFO

ABSTRACT

Lithium-ion batteries exhibit path-dependent aging behavior. Degradation mode (DM) estimation is a first step towards accurate state of health (SOH) representations by clustering degradation mechanisms. Mechanistic models shift and scale pristine half-cell open circuit potential (OCP) curves of both electrodes to reconstruct the open circuit voltage (OCV) curve by minimizing the difference between measured and reconstructed OCV. Alignment parameters describe the shift and scaling of the OCPs and can be used to estimate SOH and DMs.

---

* Corresponding author.
  E-mail address: tobias.th.hofmann@bmw.de (T. Hofmann).

Mechanistic model
Relaxed voltage points
Battery electric vehicle
Partial charging

This study introduces the *ΔQ*-method, which relies on relaxed voltage points and accumulated charge between these points. It is independent of current rates and applicable after almost every event. The optimization problem minimizes deviation between measured and reconstructed *ΔQ*. The method is developed with an automotive cell dataset and validated with real-world vehicle data from the BMW i3. The *ΔQ*-method achieves a mean absolute SOH estimation error of 2.52 % and a mean absolute OCV reconstruction error of 7.19 mV. Reliable estimations are ensured by predefined filters. The method remains effective with restricted state of charge (SOC) windows or limited data points. It is robust against variations in input data, solver choice, and optimization settings. Convergence is improved by constraining the solution space.

Nomenclature

List of Symbols

α	Scaling parameter
β	Shifting parameter
ΔQ	Charge difference between two relaxed voltage points
Δt	Time horizon of data acquisition in one data sample
ΔV	Voltage difference in one data sample
LAM	Loss of active material
LLI	Loss of lithium inventory
MAE	Mean absolute error
OCP	Open circuit potential
OCV	Open circuit voltage
SOC	State of charge
SOH	State of health
ϑ	Alignment parameter set
C	Capacity
N_{Points}	Number of points in one data sample
V	Voltage
V_{end}	Highest voltage in one data sample
V_{start}	Lowest voltage in one data sample

Subscripts

est	Estimated
FC	Full cell
interpolated	Interpolated
max	Maximum
meas	Measured
NE	Negative electrode
N	Nominal
OCV	Open circuit voltage
PE	Positive electrode
reco	Reconstructed
SOH	State of health
true	True value

Superscripts

aged	Aged
pr	Pristine

1. Introduction

With the rapid advent of battery electric vehicles (BEVs), modern battery management systems must be able to estimate internal states with high accuracy and robustness. Especially the SOH, which is commonly defined as the actual capacity in relation to the capacity at BOL, is crucial for optimal and safe operation, and prolonged battery

life. Notice about the SOH, however, does not ensure knowledge about the aging path. Lithium-ion batteries age particularly path-dependent and have strong nonlinear dependencies on their operational strategy [1–3]. Two cells with the same SOH but a different history can behave completely different in future operation. A first step towards understanding path-dependent aging are the DMs [4,5]. These modes cluster the electrochemical degradation mechanisms into loss of active material at the negative electrode (NE) (LAM_{NE}), loss of active material at the positive electrode (PE) (LAM_{PE}) and loss of lithium inventory (LLI). These modes not only allow current characterization of the cell but also a more precise future prediction and strategies to mitigate degradation [6]. The DMs are connected to the change of the OCV over lifetime and hence existing DM estimation models output the OCV as well [4,5,7]. The updated OCV is beneficial for accurate SOC estimation [8] and optimal charging strategies over lifetime. Consequently, understanding the DMs provides valuable information for accurate SOH estimation and enables proactive maintenance and control strategies.

While DM estimation models rise in popularity, numerous other SOH estimation models exist which vary in complexity and accuracy: The most common electrochemical battery model is the Newman type pseudo-two dimensional model [9–11] which needs to be modified in order to add the SOH as a solution variable. It is usually reduced in order to decrease the computational complexity. Recent reduced order models [12–14] implement the SEI-growth into an aging-dependent voltage loss equation. Other approaches [15] implement the DMs directly by adapting the stoichiometries. Either way, the parameters of interest are updated by a comparison of the modeled and measured voltage response.

With the constant rise of machine learning, it is more and more used for battery state estimation [16]. Machine learning utilizes the hidden features in measurable signals like current, voltage and temperature to exploit the correlation between these features and the SOH. Within machine learning, deep-learning gains significant attention. Especially decision-tree models, convolutional and recurrent neural networks are eligible for processing time-series data and estimating the SOH [17]. Promising publications [16,18–20] reach root-mean squared errors below 2.5 % with neural networks that process time-series data from partial charging segments. The availability of more comprehensive input data, such as electrochemical impedance spectra, has enabled even greater accuracy in estimation. For instance, Luo et al. [21] achieve a mean absolute percentage error of 1.63 % using transformer-based neural networks that leverage the electrochemical impedance spectrum. Their study demonstrates the superiority of transformer-based neural networks over recurrent neural networks in effectively processing information from complete input data or long-term data sequences.

Similar to machine learning, empirical fits use the correlation between measurable features and the SOH [22,23]. In contrast to neural networks and other ML approaches, empirical fits are designed by the engineer. These methods allow to describe the SOH as a function of multiple input signals including the operational history.

All of the aforementioned methods require data from costly and long aging studies. This major drawback makes the application of these models to new generation of cells extremely challenging, especially for fast development sequences. The mechanistic model approach, introduced by Dubarry et al. [4], however, avoids this limitation by solely relying on pristine measurement data. Hence the mechanistic model is an

efficient, cheap and non-invasive diagnostic tool. The model describes the OCV over degradation as the difference of the half-cell potentials and assumes that the OCV only changes relative to the shifting and scaling of the OCPs. How the OCPs shift and scale further determines the DMs and the SOH which allows more knowledge about the aging path.

Since the first publication of the mechanistic model approach [4], numerous papers [5,7,24–35] were published which evaluate the method for different cells including electrode composites [7,28,29] and other cost functions depending on the differential voltage analysis (DVA) or incremental capacity analysis (ICA) [26,27,30,31,33]. Schmidt et al. [7] were the first to validate the mechanistic model approach with laboratory measurements. They disassembled cells to set specific rates of LLI and LAM_{PE}. For six different cells and a C-rate below C/20, the deviation between measured and reconstructed OCPs or OCV was always below 0.5 %.

There is a noticeable increase in scientific publications [36–41] exploring the application, extension and utilization of the method at higher C-rates and during partial charging segments, making the method applicable to real-world conditions. In their study, Schindler et al. [36] demonstrated the applicability of the model to higher C-rates and varying temperatures by incorporating the Arrhenius-dependent ohmic resistance increase and rate degradation factor as additional factors. The researchers assessed the performance of the model at different C-rates (C/35, C/5, C/3) and temperatures (10 °C, 25 °C, 45 °C) and observed that the residual error in OCV reconstruction remained below 2 %. This indicates that the model provides accurate predictions even under these challenging conditions. Progress has also been made by Yang et al. [37] in the application of the method to partial charging segments from a NMC–graphite cell, even when subjected to higher C-rates. Their investigation revealed that, for a C-rate of C/3, a SOC window spanning from 20 % to 70 % is essential to achieve accurate results for various aging paths. These findings were corroborated by Chen et al. [38]: By employing DVA and ICA on C/3 partial charging segments from a NMC/LCO–graphite cell within the range of 40 % to 100 % SOC, they also successfully determined the SOH and estimated the DMs with a root mean squared error below 3.5 %. In a recent study, Schmitt et al. [39] conducted a comprehensive sensitivity analysis of the method, considering higher C-rates and varying SOC windows for a NMC–Si/graphite cell. They addressed the issue of overpotentials at higher C-rates by introducing a correction method based on subtracting constant overpotential offsets. These offsets were computed by multiplying the applied current with the measured internal resistance. Interestingly, their results diverged from those of Yang et al. [37], as they revealed that achieving accurate DM estimation requires lower C-rates ($\leq$ C/15). Furthermore, the study demonstrated that for sufficiently low C-rates ($\leq$ C/30), even partial charging segments covering the SOC range of 20 % to 70 % are adequate. For precise SOH estimation, C-rates up to C/4, and partial charging segments spanning at least the SOC window of 10 % to 80 %, were shown to be feasible [39].

Mainly due to the availability of public battery aging data and the introduction of the *alawa* toolbox [42,43] for big data generation, various machine learning approaches [44–47] using the mechanistic model approach were published. Similar to existing methods [38], these models interpret the hidden features of raw [45,47] or postprocessed [44, 46] charging curves.

The major drawback of existing methods, which rely on time-series data, is the dependency on wide SOC ranges and low C-rates. Hence, the application to real-world data is severely limited by the operational strategy of the customer.

In contrast to available methods, our novel ΔQ-method solely relies on a small number of relaxed voltage points and the accumulated charge between these points which are normally stored for BEVs. It is thus applicable to relaxed voltage points after almost every charging or driving event, independent of the applied current. This makes the ΔQ-method a promising algorithm for existing vehicle fleets.

The study at hand presents a novel algorithm for OCV reconstruction, SOH and DM estimation based on relaxed voltage points and the accumulated charge between these points. The ΔQ-method is evaluated with laboratory data from an automotive cell. The method is validated with real-world vehicle data from the BMW i3 fleet and its sensitivity to specific data filters is accessed. The influence of specific solvers and their settings is evaluated in terms of SOH error. We further highlight the advantages over conventional methods by evaluating the minimum requirements. The ΔQ-method is applicable to data from vehicles in operation with at least three measured relaxed voltage points, collected over a time-horizon up to six months. To the best of the authors knowledge, this is the first publication to design a mechanistic model approach using relaxed voltage points and accumulated charge for SOH and DM estimation.

2. Method

Knowledge about the DMs gives insight about the path-dependent aging behavior of lithium-ion batteries because the DMs correlate with the knee-point in battery aging trajectories [6]. Roeder and Ramasubramanian [48] suggested to define path dependence in three levels. While in level one, the aging path solely depends on the usage schedule, we refer in this work to level two: The current battery SOH depends on the order of usage conditions and not just their cumulative influence. As introduced by Dubarry et al. [49], extending the SOH definition with DMs helps to incorporate path-dependent battery degradation into the current state itself.

Conventional methods utilize the OCPs of the electrodes to reconstruct the full cell (FC) OCV by shifting and scaling the respective curves. Hence, it is assumed that the OCV is a function of the half cell potentials and these will only change in relation to each other which can be described by the alignment parameter set $\vartheta = [\alpha_{NE}, \alpha_{PE}, \beta_{NE}, \beta_{PE}]$. The α-parameters specify the squeezing and the β-parameters describe the shifting of the OCPs. If the OCPs or the OCV are captured at very low C-rates, they are pseudo-OCP/OCV because even at low C-rates the measured values will deviate from the truly relaxed voltage. For simplicity, in the following the terms pseudo-OCP/OCV and OCP/OCV will be used as synonyms.

2.1. Method description

Along a battery's lifetime its OCPs can be described with respect to the electrode SOC (SOC_{NE} and SOC_{PE}) or charge amount

$$OCP_{NE} = f_{NE}(SOC_{NE}) \tag{1}$$

$$OCP_{PE} = f_{PE}(SOC_{PE}). \tag{2}$$

Fig. 1 summarizes the steps to set up the algorithm: First, the OCV and OCPs must be captured in either charge or discharge direction. The direction of charge should be kept constant throughout the application of the algorithm to reduce the influence of hysteresis. All curves are normalized to their respective SOC. The C-rate is usually set below C/20 to decrease the influence of overpotentials. All inputs are transformed into the coordinate system of the full cell, i.e., the full cell SOC (SOC_{FC}), by scaling the specific electrode SOCs by the α-parameter and finally shifting them by the β-parameter.

$$SOC_{FC} = \alpha_{NE} \cdot SOC_{NE} + \beta_{NE} \tag{3}$$

$$SOC_{FC} = \alpha_{PE} \cdot SOC_{PE} + \beta_{PE} \tag{4}$$

Hence, Eqs. (1) and (2) transform to

$$OCP_{NE} = f_{NE}((SOC_{FC} - \beta_{NE})/\alpha_{NE}) = f_{NE}(SOC_{FC}, \vartheta) \tag{5}$$

$$OCP_{PE} = f_{PE}((SOC_{FC} - \beta_{PE})/\alpha_{PE}) = f_{PE}(SOC_{FC}, \vartheta). \tag{6}$$

The full mathematical derivation of the coordinate transformation can be found in the publication by Schmitt et al. [39].
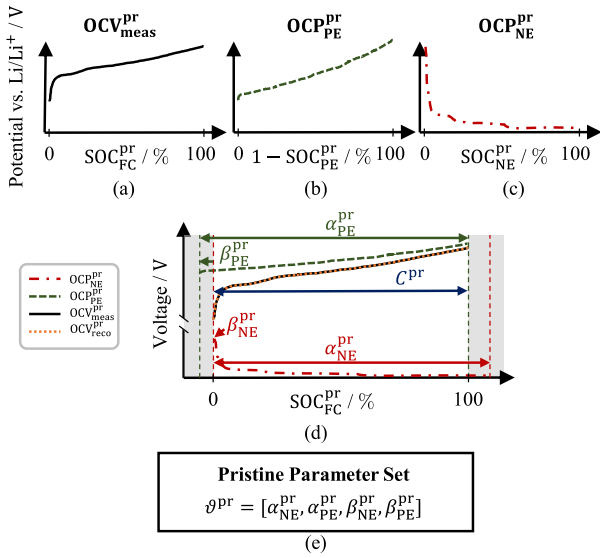
Fig. 1. Initialization process of conventional OCV reconstruction models. The OCV (a) together with the positive (b) and negative (c) electrode OCPs in the pristine state are captured at the same C-rate. In this example, all curves are measured in charge direction. (d) The pristine alignment parameters are fitted to minimize the error between the pristine OCV measurement and the reconstructed curve. (e) The resulting pristine alignment parameters are later mandatory to derive the SOH and DMs.

Finally, the OCV can be described with the help of the OCPs and the alignment parameters

$$OCV(SOC_{FC}) = f_{FC}(OCP_{NE}, OCP_{PE}, \vartheta, SOC_{FC}). \tag{7}$$

Second, the pristine (pr) alignment parameters are fitted to minimize the error between the measured (meas) and reconstructed (reco) OCV curve OCV_{meas} and OCV_{reco}. The cell's BOL capacity is defined as the accumulated charge between the minimum and maximum cell voltage. Per definition, the SOH is always 100 % for this scenario. Last, the pristine alignment parameter set ϑ^{pr} must be stored in order to calculate the DMs in the application phase. In Fig. 2 the application phase is visualized for the conventional but also the ΔQ-method. The conventional algorithm, illustrated in Figs. 1 and 2, takes the raw OCV measurement OCV_{meas} (Fig. 1a) and the pristine OCPs: $OCP^{pr}_{PE,meas}$, $OCP^{pr}_{NE,meas}$ (Fig. 1b and c) as an input. By shifting and scaling the OCPs in relation to each other, the OCV reconstruction error is minimized (Fig. 1d) to finally yield the alignment parameters (Fig. 1e) and hence the SOH and DMs. Advances are made to use DVA and ICA for optimization [36–38]. The optimization happens in the coordinate system of the pristine full cell SOC (SOC^{pr}_{FC}) or the absolute Ah-space. If a local optimum is found and no further feasible direction is detectable, the algorithm stops and returns the aged alignment parameter set

$$\vartheta^{aged} = \arg\min_{\vartheta} \|OCV_{meas}(SOC_{FC}) - OCV_{reco}(\vartheta, SOC_{FC})\|_2. \tag{8}$$

The choice of optimization algorithm, i.e., gradient descent, particle swarm or genetic algorithm, can influence the final parameter solution.

In contrast to conventional methods, the ΔQ-method requires only three measured relaxed voltage points V_1, V_2, V_3 and the accumulated charge between these points $\Delta Q_1, \Delta Q_2$. By definition, the ΔQ is positive for charging events. For negative ΔQs and consequently discharge events, the ΔQ is inverted and the order of the voltage pair is reversed to meet the requirements. The algorithm minimizes the objective function $f(\vartheta)$, which is the vector of accumulated charge between adjacent points, and fixates the OCV points

$$\vartheta^{aged} = \arg\min_{\vartheta} \|f(\vartheta)\|_2$$
$$= \arg\min_{\vartheta} \|\Delta Q_{meas}(V) - \Delta Q_{reco}(\vartheta, V)\|_2, \tag{9}$$

where ΔQ_{meas} is the vector of measured ΔQs and ΔQ_{reco} is the vector of the reconstructed ΔQs.

Instead of optimizing with respect to the y-axis, the ΔQ-method uses the x-axis. One of its advantages lies in the fact that no fixed reference voltage is required. Hence, every voltage pair is fitted individually. The alignment parameters not only yield the aged OCV-curve (Eq. (7)) but are further used to calculate the DMs. Because the aged OCV is reconstructed in the charge coordinate system, the SOH is easily derived by Eq. (10). The capacity of the pristine cell C^{pr} is simply the accumulated charge between the voltage limits for the pristine fit in Fig. 1d. The same applies for the estimated capacity of the aged cell C^{aged}_{est}.

$$SOH = \frac{C^{aged}_{est}}{C^{pr}} = \frac{Q^{aged}(V^{aged}_{max})}{Q^{pr}(V^{pr}_{max})} \tag{10}$$

In Eq. (10), Q^{aged} and Q^{pr} are the aged and the pristine charge vector, while V^{aged}_{max} and V^{pr}_{max} are the maximum voltage values of the aged and pristine voltage curves.

Loss of active material describes the available electrode capacity with respect to the pristine state. For both electrodes, the definition is similar:

$$LAM_{NE} = \frac{\alpha^{pr}_{NE} - \alpha^{aged}_{NE}}{\alpha^{pr}_{NE}} \tag{11}$$

$$LAM_{PE} = \frac{\alpha^{pr}_{PE} - \alpha^{aged}_{PE}}{\alpha^{pr}_{PE}} \tag{12}$$

Lithium inventory C_{lit} is the available lithium for cycling in both electrodes, i.e. the superposition of both OCPs. The loss of lithium inventory is defined with respect to the pristine amount of available lithium inventory C^{pr}_{lit}.

$$LLI = \frac{C^{pr}_{lit} - C_{lit}}{C^{pr}_{lit}} \tag{13}$$

When examining both OCPs across the entire delithiation and lithiation range, it is observed that the cathode builds a capacity overhang during discharge, while the anode exhibits a capacity overhang during charge [5], as depicted in Fig. 1. This remains generally true throughout the lifespan, leading to the definition of lithium inventory primarily as

$$C_{lit} = (\alpha_{PE} + \beta_{PE} - \beta_{NE}) \cdot C_N. \tag{14}$$

There are instances, however, where the minimum or maximum lithiation degree for the initial measurement deviates from the standard definition due to varied measurement settings. This results in the possibility of mathematically determining an overhang in the discharge direction for the anode or an overhang in the charge direction for the cathode. In Fig. 4(a) for example, the cathode is limiting in charge and discharge direction. Besides the deviations in initial measurement settings, even if the pristine alignment parameters are set as in Fig. 1, a rapid LAM_{NE}, without LAM_{PE} and LLI, may lead to the need for a new lithium inventory definition. Hence, it becomes necessary to introduce a case-sensitive definition for the lithium inventory, as shown in Eq. (15).

$$C_{lit} = \begin{cases} (\alpha_{PE} - \beta_{NE} + \beta_{PE}) \cdot C_N & \text{, for } (\alpha_{PE} + \beta_{NE} - \beta_{PE}) < \alpha_{NE} \\ & \wedge \ (\beta_{PE} - \beta_{NE}) \leq 0 \\ (\alpha_{NE} - \beta_{NE}) \cdot C_N & \text{, for } (\alpha_{PE} + \beta_{NE} - \beta_{PE}) > \alpha_{NE} \\ & \wedge \ (\beta_{PE} - \beta_{NE}) \leq 0 \\ (\alpha_{NE} + \beta_{NE} - \beta_{PE}) \cdot C_N & \text{, for } (\alpha_{NE} + \beta_{NE} - \beta_{PE}) < \alpha_{PE} \\ & \wedge \ (\beta_{PE} - \beta_{NE}) \geq 0 \\ (\alpha_{PE} - \beta_{PE}) \cdot C_N & \text{, for } (\alpha_{NE} + \beta_{NE} - \beta_{PE}) > \alpha_{PE} \\ & \wedge \ (\beta_{PE} - \beta_{NE}) \geq 0 \end{cases} \tag{15}$$
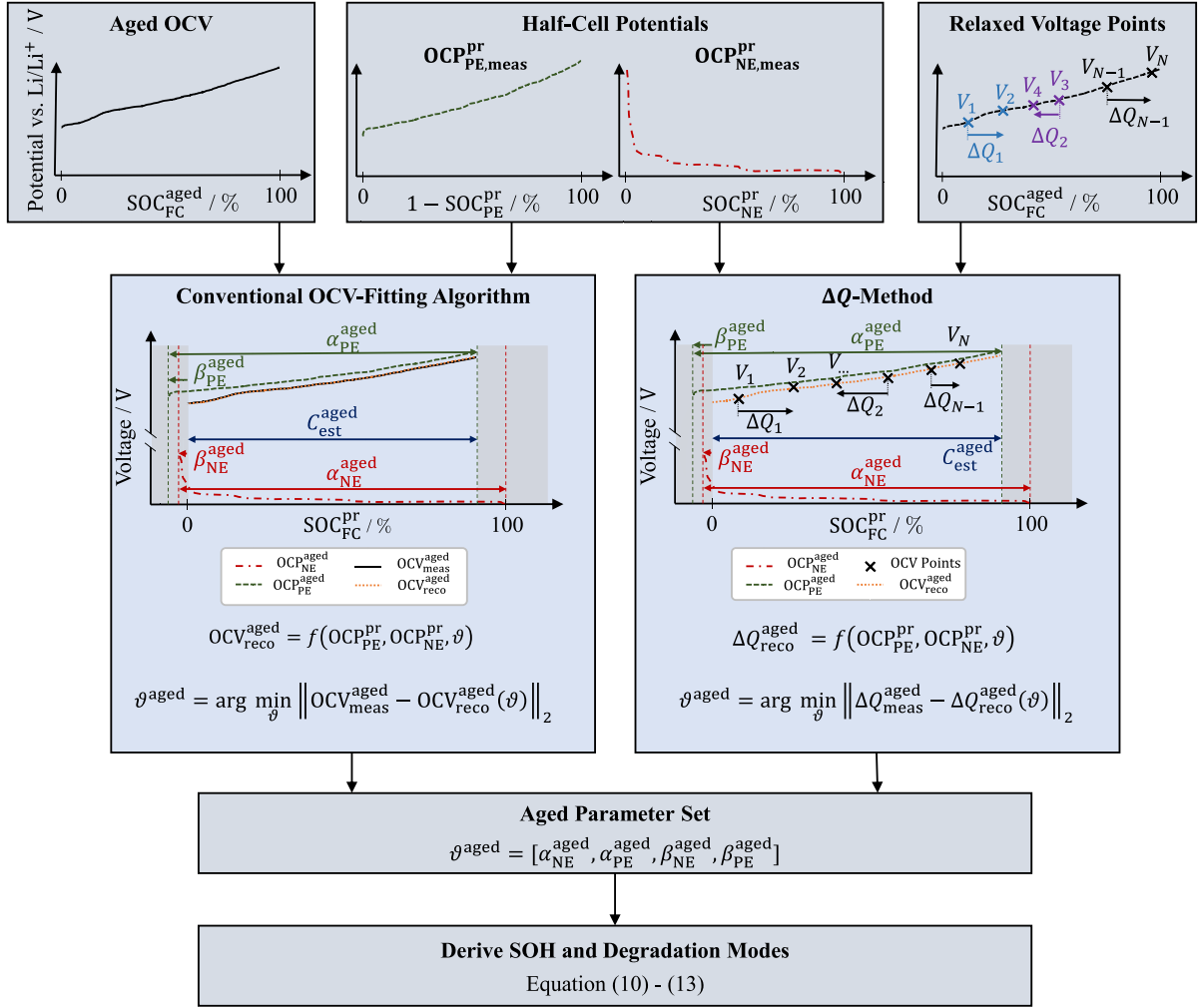
Fig. 2. Description of conventional OCV reconstruction methods and the novel ΔQ-method. For both algorithms the pristine OCPs are mandatory. While conventional methods use time-series measurements of the OCV, the ΔQ-method solely requires relaxed voltage points and the accumulated charge between those points. Conventional methods fit the pristine OCPs to the measured OCV by shifting and scaling the curve to minimize the OCV reconstruction error. The ΔQ-method, however, pursues the same target by minimizing in respect to the x-axis, i.e., the accumulated charge between two relaxed voltage points. The optimization argument yields the optimal alignment parameters which are used to estimate the SOH and DM.

2.2. Dataset

This paper introduces the basic idea of the ΔQ-method. First, the method is developed with measurements under laboratory conditions from a cyclic aging study of an automotive cell. The used automotive cell has a NMC811-cathode, a graphite-anode and a nominal capacity of 116 Ah [50]. Second, the developed algorithm is applied to real-world vehicle field data from the BMW i3, which was captured over eight years, not relying on accelerated aging tests. The BMW i3 uses a different cell with a NCA/NMC/LMO-blended-cathode, a graphite-anode and a nominal capacity of 60 Ah measured by a constant-current constant-voltage (CCCV) charge with C/3 at 25 °C.

The cell dataset comprises of twelve samples with 27 relaxed voltage points, the accumulated charge between these points and the respective SOH$_{\text{true}}$ label. All points were measured at 25 °C in charge direction. Half of the samples were taken at BOL, while the remaining samples are distributed between 77 % to 93 % SOH after performing 500 to 1000 continuous cycles with C/3 charge and C/2 discharge at 10 °C and 35 °C. The pristine, true alignment parameter set is known from a previous publication [50] investigating the same cell.

In contrast to the standardized cell dataset, the vehicle dataset is captured at various conditions for 574 vehicles. The vehicle dataset is visualized in Fig. 3 with special focus on the variables of interest:

SOH, number of relaxed voltage points, voltage level and accumulated charge between two adjacent voltage points. While the signals voltage and charge were captured on pack level, they are transformed to cell-level by multiplication by a fixed scaling factor. All vehicles in this dataset have undergone at least one and a maximum of eight testbench capacity measurements to create the SOH$_{\text{true}}$ label. The testbench capacity measurement consists of a CCCV charge with C/3 at the service. The capacity is defined as the full accumulated charge throughput during this service. The dataset is categorized into three degradation states based on mileage: BOL for vehicles with mileage below 25 000 km, MOL for vehicles with mileage between 25 000 km and 100 000 km, and EOL for vehicles with mileage exceeding 100 000 km. The total mileage correlates with the aging state of the high voltage storage system. The SOH remains above 75 % even for vehicles with over 100 000 km and a vehicle age above eight years. While all BOL vehicles have a SOH above 90 % and all EOL vehicles have a SOH below 85 %, the MOL vehicles show ranges over the entire extreme, where one can see more clearly the influence of other factors on the vehicle SOH. The dataset was recorded within a time window of eight years. As a result, not every historical relaxed voltage point is included in the dataset. For this dataset, BOL vehicles are operated more frequently than MOL or EOL vehicles and inhibit more data points. Regarding voltage levels and SOC, the majority of data points in the entire dataset
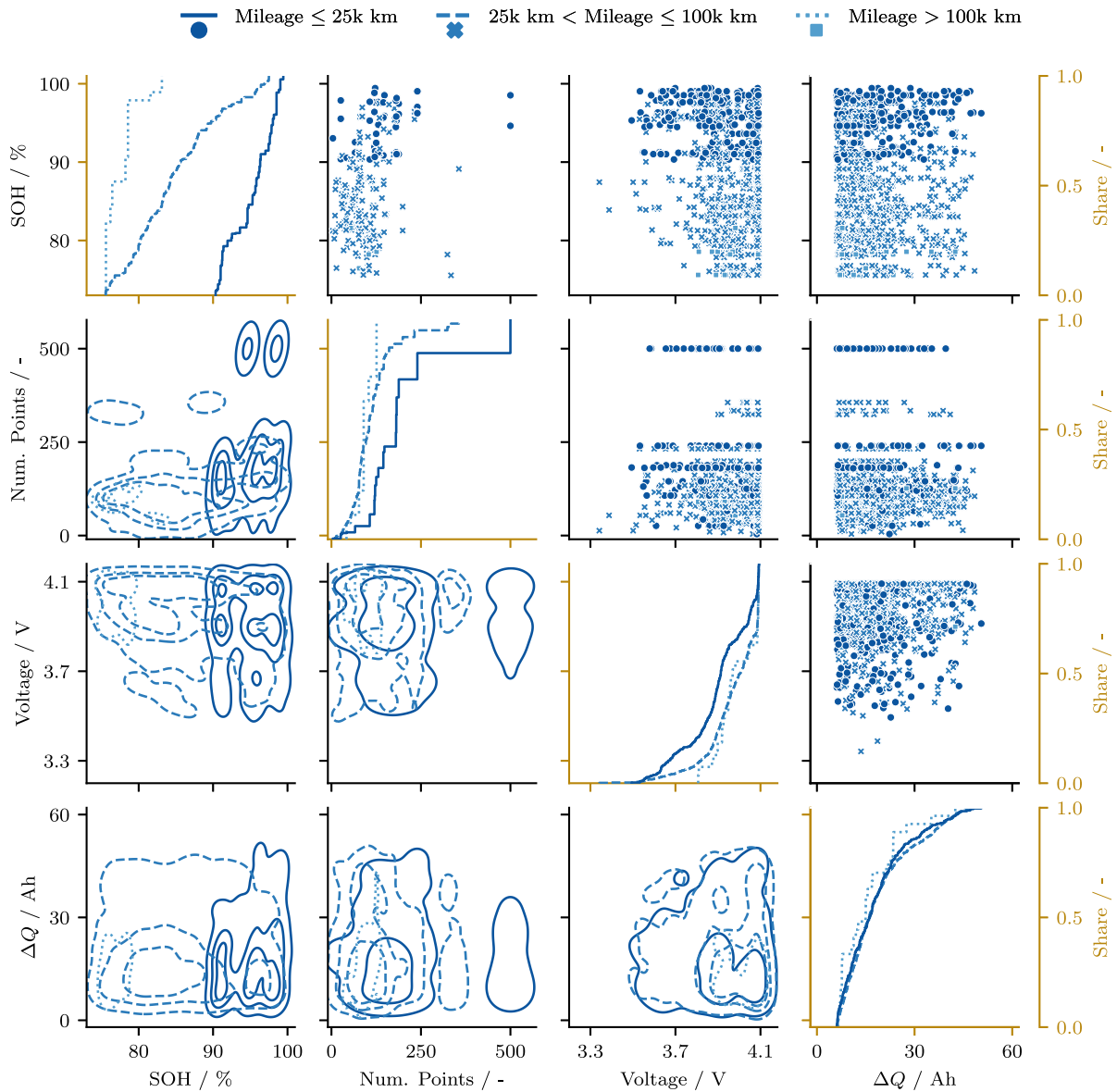
Fig. 3. Visualization of the validation dataset gathered from aged vehicles in the field. The upper diagonal figures show the scatter plot and the lower diagonal figures visualize the kernel densities. Both refer to the first *y*-axis on the left. The second *y*-axis on the right side refers to the cumulative distribution plots in the diagonal, in golden color. The hue indicates the milage of the investigated vehicles, which shows good agreement with the SOH.

are distributed at higher voltage levels. This observation is reasonable since there is high probability that a relaxed voltage point is recorded after a charging event. Due to the relatively small capacity of the first BMW i3, customers tended to show high frequent charging behavior. Additionally, the OCV increases with degradation, leading to even more data points at higher voltage levels. The accumulated charge between two adjacent points provides insights into user behavior. A higher value indicates longer charging events or that the vehicle is operated for a longer duration between stops. Comparing these key charging features, the cumulative distribution exhibits remarkable similarity for all three datasets, implying that user behavior remains consistent over the lifetime of the vehicles.

The dataset does not include the history between two points, i.e., current profile or the temperature, but makes sure that between two points charging events are not mixed with driving events. The combination of OCV points derived from both charging and discharging events, irrespective of their prior history, may be achieved under negligible hysteresis assumptions for the given cell. This objective can

be realized by assigning a positive ΔQ value to a charging event, and multiplying the discharge event, which yields a negative ΔQ, by -1. To this end, the order of the measured voltage pair needs to be reversed.

3. Results

The proposed method is first implemented on cell data. The developed method is validated with actual field data from the BMW i3, which uses a different cell.

3.1. Application of the method to laboratory cell data

Fig. 4 provides a comprehensive visualization of the complete application of the ΔQ-method. In Fig. 4(a), the pristine OCPs, OCV, and measurement results are depicted. Additionally, the interpolation of the OCV voltage points is included to enhance the visualization of the actual OCV trajectory. The OCPs are appropriately adjusted based on their corresponding pristine alignment parameters, which are
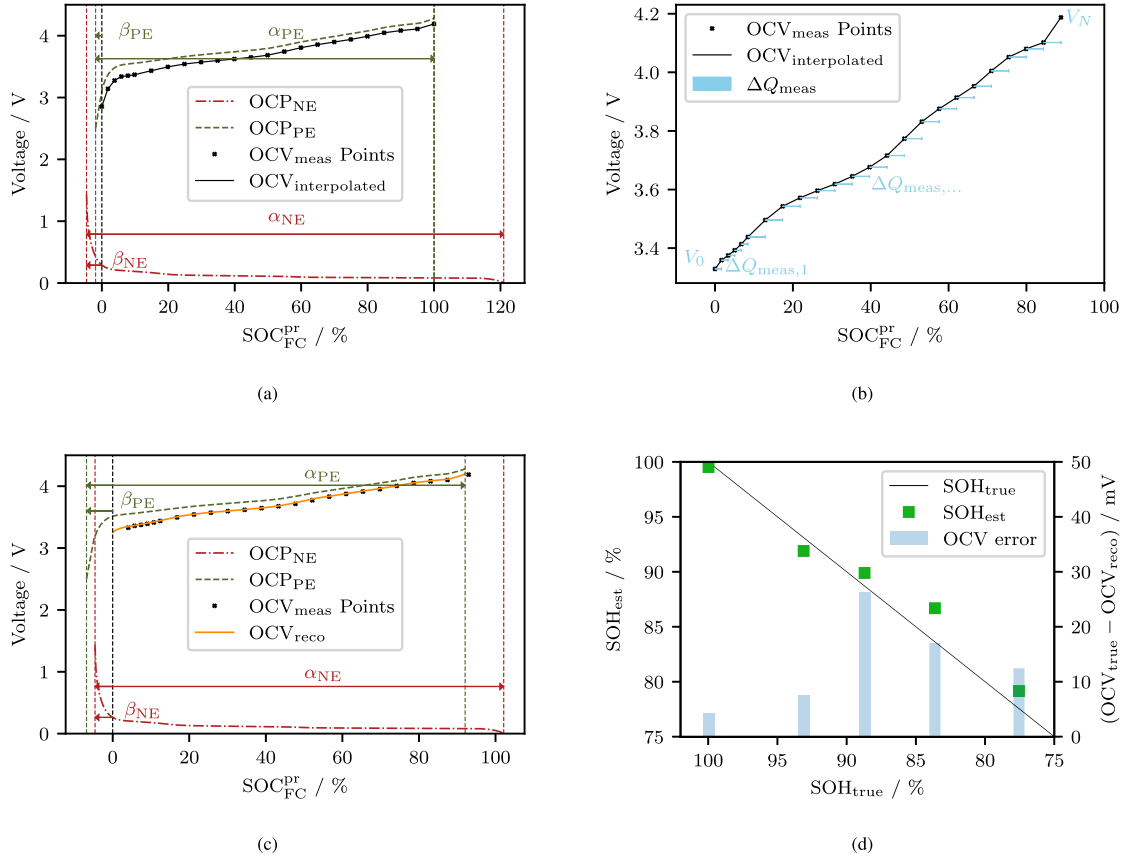
Fig. 4. Application of the algorithm to a single sample at an aged state from the standardized cell dataset. (a) Pristine Fit for investigated cell. (b) Input for ΔQ-algorithm: aged relaxed OCV points with accumulated charge between points. (c) Optimization result for aged cell. For this cell: $\mathrm{MAE_{SOH}} = 1.05\,\%$ and OCV reconstruction error: $\mathrm{MAE_{OCV}} = 12.4\,\mathrm{mV}$. (d) Result for all samples: $\mathrm{MAE_{SOH}} = 1.11\,\%$ and OCV reconstruction error: $\mathrm{MAE_{OCV}} = 9.09\,\mathrm{mV}$.

given in Table 1. In this paper all alignment parameters refer to a normalized SOC-axis between zero and one. It is worth noting that the observed anode-overhang in the discharge direction, as discussed earlier, is a result of the high cutoff voltage set to 1.5 V during the $\mathrm{OCP_{NE}}$ measurement.

Fig. 4(b) illustrates the relaxed voltage measurements obtained from an aged cell. Again, an interpolation of the voltage points is visualized.

In order to apply the algorithm, the data needs to undergo preprocessing and to be organized into a matrix where the columns contain a vector with the voltage and charge difference value pairs, with each row representing a complete set for a sample at a consistent SOH. Specifically, the voltage points V_1 and V_2 are set in the first column, along with the corresponding charge difference $\Delta Q_1 = Q(V_2) - Q(V_1)$. Subsequently, the second column is filled with V_3, V_4, and $\Delta Q_2 = Q(V_4) - Q(V_3)$, as shown in Eq. (16).

$$\begin{bmatrix} V_1 & V_2 & \Delta Q_1 \\ V_3 & V_4 & \Delta Q_2 \\ \dots & & \end{bmatrix} \tag{16}$$

Again, if for example ΔQ_1 is negative due to a driving event, Eq. (16) changes, as in Eq. (17).

$$\begin{bmatrix} V_2 & V_1 & -\Delta Q_1 \\ V_3 & V_4 & \Delta Q_2 \\ \dots & & \end{bmatrix} \tag{17}$$

For the cell laboratory measurements V_3 equals V_2 and so forth. Along with the measured data, the pristine OCPs are normalized to equal length and stored to be used within the optimization process.

Table 1
Alignment parameter for the pristine state (SOH=100 %) and the estimation for an aged cell (SOH=93 %) (sample from Fig. 4(c)).

	α_{NE}	α_{PE}	β_{NE}	β_{PE}
Pristine	1.26	1.02	−0.05	−0.02
Aged Estimation	1.07	0.99	−0.05	−0.07

The optimization problem is formulated within MATLAB and the built-in nonlinear least-squares solver *lsqnonlin()* [51]. Instead of minimizing a scalar value, the nonlinear least-squares solver minimizes the vector of differences, as in Eq. (9). The default algorithm *trust-region-reflective* and all default settings from MATLAB are used for the solver [51]. The settings must be further redefined for more challenging datasets, i.e., the BMW i3 dataset in the consecutive subsection.

The optimization constraints and initial start points are set according to Table 2, which were found to be the best fit for pristine state and reflect most of the battery degradation. The algorithm does not rely on any additional constraints except the lower and upper boundaries.

Defining broader boundaries which make up to the full SOH-range lead to several local optima and the high risk of returning a result with an optimal solution with respect to the loss function but unreasonable alignment parameters. This means that for a specific set of voltage points several combinations of parameters exist which lead to equally low cost values of the objective function. Nevertheless, just a single combination yields the correct result. Limiting the solution space with adequate constraints helps to marginalize unwanted local optima.

The objective function $f(\vartheta)$, as it appears in Eq. (9), is defined as the vectorized difference between the measured $\Delta Q_{\mathrm{meas}}(V)$ and the

Table 2
Optimization constraints and initial values of the *lsqnonlin()* solver for the cell dataset.

Parameter	α_{NE}	α_{PE}	β_{NE}	β_{PE}
	BOL			
Initial Value	1.23	1.00	−0.05	−0.04
Lower Bound	1.21	0.99	−0.05	−0.04
Upper Bound	1.26	1.02	−0.05	−0.02
	MOL			
Initial Value	1.13	0.92	−0.05	−0.04
Lower Bound	1.07	0.87	−0.07	−0.07
Upper Bound	1.22	0.99	−0.05	−0.02
	EOL			
Initial Value	0.98	0.80	−0.05	−0.02
Lower Bound	0.94	0.76	−0.07	−0.07
Upper Bound	1.02	0.83	−0.05	−0.02

BOL: SOH $\geq$ 95 %, MOL: 80 % $\leq$ SOH < 95 %, EOL: SOH < 80 %.

reconstructed $\Delta Q_{\text{reco}}(\vartheta, V)$. Because all charge vectors are consecutive, i.e., in Eq. (16) V_3 equals V_2 and so forth, the optimization problem can be further simplified.

$$f(\vartheta) = \Delta Q_{\text{meas}}(V) - \Delta Q_{\text{reco}}(\vartheta, V)$$

$$= \begin{bmatrix} f_1(\vartheta) \\ f_2(\vartheta) \\ \cdots \\ f_{N-1}(\vartheta) \end{bmatrix} = \begin{bmatrix} \Delta Q_{\text{meas},1} - \Delta Q_{\text{reco},1} \\ \Delta Q_{\text{meas},2} - \Delta Q_{\text{reco},2} \\ \cdots \\ \Delta Q_{\text{meas},N-1} - \Delta Q_{\text{reco},N-1} \end{bmatrix}$$

$$= \begin{bmatrix} (Q_{\text{meas},2} - Q_{\text{meas},1}) - (Q_{\text{reco}}(V_2, \vartheta) - Q_{\text{reco}}(V_1, \vartheta)) \\ (Q_{\text{meas},3} - Q_{\text{meas},3}) - (Q_{\text{reco}}(V_3, \vartheta) - Q_{\text{reco}}(V_2, \vartheta)) \\ \cdots \\ (Q_{\text{meas},N} - Q_{\text{meas},N-1}) - (Q_{\text{reco}}(V_N, \vartheta) - Q_{\text{reco}}(V_{N-1}, \vartheta)) \end{bmatrix} \quad (18)$$

The nonlinear least-squares problem is

$$\vartheta_{\text{est}} = \arg\min_{\vartheta} \| f(\vartheta) \|_2^2$$

$$= \arg\min_{\vartheta} (f_1(\vartheta)^2 + f_2(\vartheta)^2 + \cdots + f_{N-1}(\vartheta)^2) \quad \text{s.t.} \quad (19)$$

$$\vartheta \geq \text{lb}$$
$$\vartheta \leq \text{ub}$$

where lb is the lower and ub is the upper boundary, according to Table 2.

Fig. 4(c) shows the optimization result for the sample in Fig. 4(b). The alignment parameters change according to Table 1.

With Eqs. (10), (11), (12) and (15) the SOH and DMs can be calculated. According to Table 2 the highest reachable DMs are 25.4 % for LAM_{NE}, 25.5 % for LAM_{PE} and 27.9 % for LLI. For the sample in Fig. 4(c) the estimated SOH is 92.1 %, which underestimates the actual SOH by absolute 1.05 %. $\text{LAM}_{\text{NE, est}}$ is 20.6 %, $\text{LAM}_{\text{PE, est}}$ is 16.7 % and LLI, est is 19.1 %. Mainly LAM_{PE} is responsible for LLI due to the anode overhang and the negligible relative shift of the OCPs. Further, LLI highly correlates with the SOH fade once the capacity overhangs of the anode is consumed, i.e., LAM_{NE} exceeds 16.7 %. If the cathode OCP does not shift, every LAM_{PE} directly leads to LLI and consequently to a decreasing SOH. The OCV reconstruction error is 12.4 mV. While SOH and OCV estimation is validated with the true value, it is not evaluated for the DMs. A detailed validation of the DM estimation exceeds the scope of this publication.

Fig. 4(d) presents the final result for all eleven samples of the cell dataset. All results are evaluate in terms of the mean absolute error (MAE). The MAE is defined as

$$\text{MAE} = \frac{1}{N} \sum_{i=1}^{N} \left| Y - \hat{Y} \right| \quad (20)$$

where Y is the true value, $\hat{Y}$ is the estimate and N is the total number of samples.

The MAE of SOH estimation is 1.11 % and the OCV MAE is 9.09 mV. The green squares show the estimated versus the true SOH. Due to the small amount of samples per SOH-value and the similar estimation result of those samples, the standard deviation is too small to be visible. The light blue bars indicate the OCV reconstruction error. While the estimation accuracy of SOH and OCV is very high for samples above 90 %, it decreases for higher degraded cells. The OCV error seems to directly correlate with the SOH error. Although this trend can be generally observed in Fig. 4(d), the samples with a true SOH of 88 % show the highest OCV error, while the SOH error is smaller than average.

For the laboratory dataset, one set of boundary conditions and a fixed initial start point, i.e., using the BOL upper boundary, EOL lower boundary, and MOL initial point, leads to accurate results. The reconstruction algorithm achieves a SOH MAE of 1.29 % (+0.18 % compared to clustered conditions, Fig. 4(d)) and an OCV reconstruction MAE of 9.70 mV(+0.61 mV compared to clustered conditions, Fig. 4(d)).

3.2. Validation of the method with vehicle field data

To evaluate the commercial viability, the proposed algorithm is validated with actual field data from the BMW i3. This dataset, on the one side, includes more samples and increases statistical significance. On the other side, the more challenging boundary conditions prove the real-world applicability of the ΔQ-method.

Fig. 5 gives a brief summary of the algorithm workflow, the dataset and the final result. As shown in Fig. 5(a), the method starts with an existing testbench capacity measurement as a reference. For this specific vehicle, a set of relaxed voltage points and the accumulated charge information are accessed. This dataset is preliminary checked and filtered to align with the requirements. The preset filters are a result of an availability-accuracy tradeoff, which is discussed in detail in Section 4. At least 10 data points, captured within the last 25 to 40 days before the testbench capacity measurement, must be available. The time horizon extends with higher vehicle age, i.e., older vehicles are closer to 40 on average. Additionally, the vehicle must be above 75 % SOH to align with the preset alignment parameter boundaries in Table 3. This criterion is simply checked by assessing the previous testbench capacity measurement. If no earlier measurement is available, the criterion is always fulfilled. For the investigated vehicle dataset, however, barely any samples below 75 % are available (see Fig. 3). Hence, this filter excludes a negligible amount of EOL vehicles. If all criteria are met, the boundary conditions of the algorithm are set according to Table 3. To prefilter the boundary conditions, the last maximum onboard (ob) SOH estimation $\max(\text{SOH}_{\text{ob}})$ is used as a criterion. This values is generally available and accurate enough to distinguish between BOL, MOL and EOL, but limited due to computing resources. The ΔQ-method processes this information and increases the quality and reliability of estimation. The ΔQ-method is validated against testbench capacity measurements instead of the onboard estimation.

The boundary conditions per degradation state are set such that they have an overlap with the other degradation states. This means, even if the latest maximum SOH onboard estimate implies that the boundary conditions are set according to BOL-conditions, the final estimate can still lay in the MOL-range. Hence, rough preliminary knowledge about the vehicle age is enough to run the algorithm. As shown with Eq. (19), the optimization uses the pristine OCPs to reconstruct the most accurate voltage curve. The optimization returns the adopted OCV, which is essential to estimate the SOH (Eq. (10)). In combination with the pristine parameter set, the estimated parameter set yields the DMs (Eqs. (11), (12), (15)).

In comparison to the cell dataset, the vehicle data demand tuned settings, as given in Table 3. The specific settings are a result of a detailed sensitivity analysis, which is further discussed in Section 4.

The maximum function evaluations (MaxFunEvals) are reduced to 100 from the default value of 400 to decrease the time-effort but
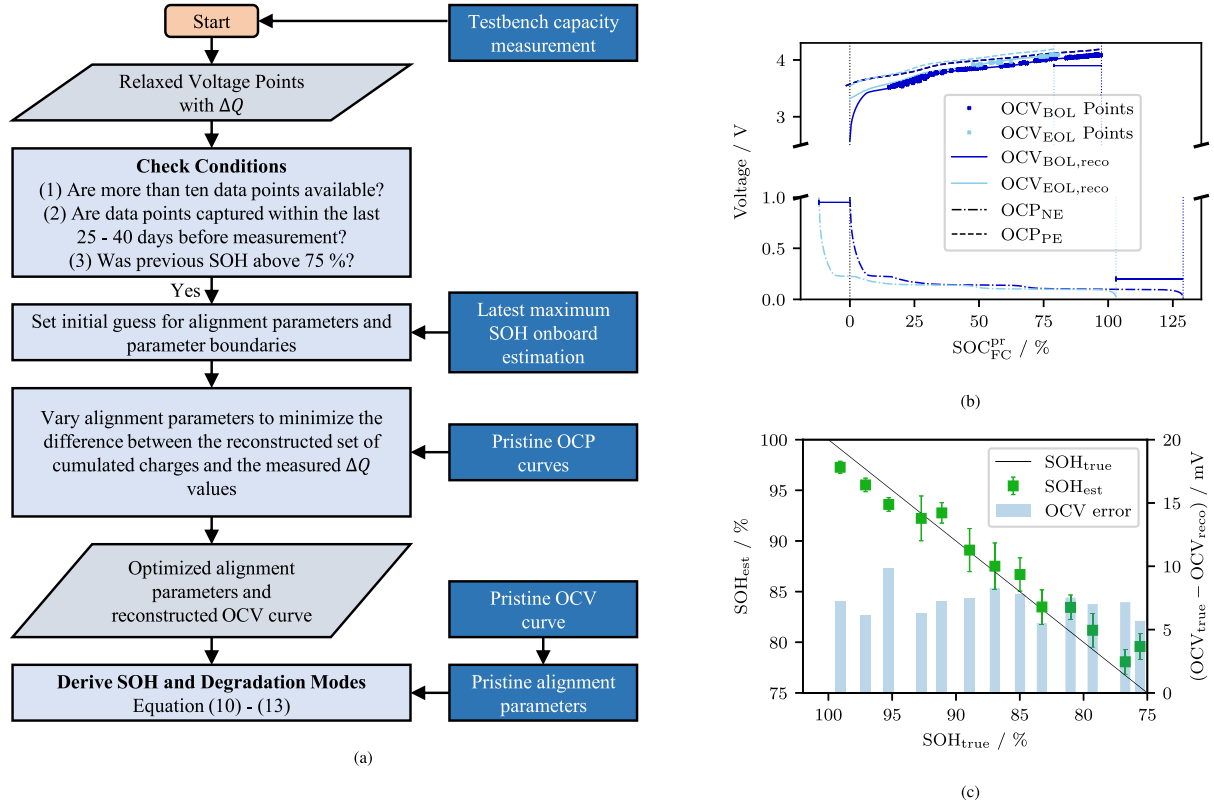
Fig. 5. Application of the algorithm to the vehicle dataset. (a) Workflow of the *ΔQ*-method. Input fields are colored in dark blue. (b) Input samples and optimization results for a BOL and EOL measurement. The arrows indicate the shift of the half cell potentials due to LAM and LLI. It must be noted that the cathode OCP was measured within a narrow voltage range leading to the appearance of a limiting cathode in discharge direction for the EOL sample. (c) Result for all samples: $MAE_{SOH} = 2.52\%$ and OCV reconstruction error: $MAE_{OCV} = 7.19\,mV$. The OCV reconstruction error is solely calculated in respect to the measured points which are used for the fitting process.

Table 3

Optimization settings, constraints and initial values of the *lsqnonlin()* solver for the BMW i3 vehicle dataset. The criteria for the BOL, MOL and EOL condition is realized by accessing the latest maximum SOH onboard estimation.

Setting	Value			
MaxFunEvals	100			
DiffMaxChange	1×10^{-5}			
DiffMinChange	1×10^{-5}			
FinDiffType	central			
Parameter	α_{NE}	α_{PE}	β_{NE}	β_{PE}
	BOL			
Initial Value	1.29	1.01	−0.10	0.00
Lower Bound	1.16	0.96	−0.16	−0.02
Upper Bound	1.29	1.01	0.00	0.00
	MOL			
Initial Value	1.23	0.91	−0.15	0.00
Lower Bound	1.16	0.77	−0.19	0.00
Upper Bound	1.25	0.96	−0.06	0.00
	EOL			
Initial Value	1.16	0.81	−0.16	0.00
Lower Bound	0.97	0.76	−0.20	0.00
Upper Bound	1.23	0.91	−0.08	0.00

BOL: $\max(SOH_{ob}) \geq 95\%$, MOL: $80\% \leq \max(SOH_{ob}) < 95\%$,
EOL: $\max(SOH_{ob}) < 80\%$.

Table 4

Alignment parameter for the pristine state (SOH=100%) and the estimation for an aged storage (SOH=80%, sample from Fig. 5(b)).

	α_{NE}	α_{PE}	β_{NE}	β_{PE}
Pristine	1.29	1.02	0.00	−0.02
Aged Estimation	1.15	0.79	−0.12	0.00

While these tuned settings lead to a marginal SOH-estimation accuracy increase, they drastically reduce runtime: The MAE_{SOH} reduces from 2.57% to 2.52% and the computation time decrease by 41.5%, on average.

As can be seen, the boundaries of the degradation states overlap, to make up for imprecise classification by the latest maximum SOH onboard estimation. The maximum reachable DMs are 24.8% for LAM_{NE}, 25.5% for LAM_{PE} and 26.9% for LLI. The pristine alignment parameter set is given in Table 4. It further includes the parameter estimation result for the aged sample of Fig. 5(b).

Fig. 5(b) reveals the optimization result for a BOL and EOL sample. The BOL sample is estimated with an absolute SOH error of 1.82% and underestimates the value to be at 97.2%. Nevertheless, the OCV reconstruction error stays below 5.62 mV which indicates an accurate fit. The EOL sample reaches an absolute SOH error of 0.13% and the OCV reconstruction error is 8.21 mV. The alignment parameters in Table 4 yield the DMs: The $LAM_{NE,\,est}$ is 11.2%, the $LAM_{PE,\,est}$ is 22.4% and the LLI_{est} adds up to 22.4%. Due to the oversized anode, the LLI_{est} approximately equals $LAM_{PE,\,est}$ and leads to the estimated SOH of 80%, which is further visible in Fig. 5(b). It must be noted that the anode overhang in discharge direction for the EOL sample may appear due to the limited voltage range for the cathode OCP measurement. On the contrary, this type of degradation is possible, following the

still allow convergence. The minimum change in finite-difference for the variables (DiffMinChange) increases from zero to 1×10^{-5}. The maximum change (DiffMaxChange) is reduced from infinity to the same value as DiffMinChange, 1×10^{-5}. These settings allow fast computation while significant optimization steps are performed. It further hinders the algorithm from taking too large steps and potential skipping of optima. The finite difference type (FinDiffType) is switched from forward to centered, which doubles function evaluations but increases accuracy.
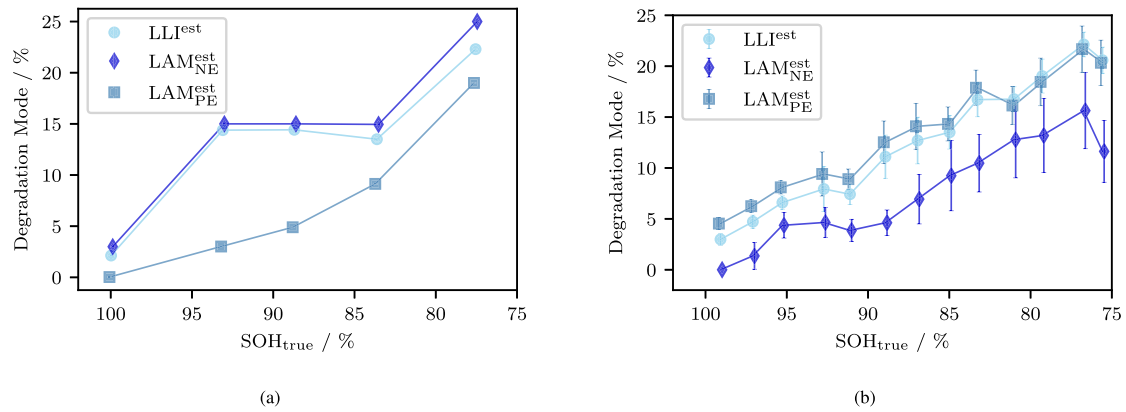
Fig. 6. Evolution of the DMs and their standard deviation, clustered per 2 % SOH range, for the (a) cell dataset and the (b) vehicle dataset. The markers for the LAM modes are slightly shifted to the left and right of the true SOH value in order to increase visibility.

explanations by Birkl et al. [5], who contribute this type of electrode shifting to delithiated LAM_{PE}.

The evaluation for the full dataset is presented in Fig. 5(c). The ΔQ-method achieves reasonable results with an MAE_{SOH} of 2.52 % against the testbench capacity measurements and an MAE_{OCV} of 7.19 mV. The standard deviation implies high estimation confidence for a broad spectrum of vehicles. For the larger and more diverse i3 dataset, the correlation of SOH and OCV accuracy is less prominent.

4. Discussion

One big advantage of the proposed method (or in general, the mechanistic model approach [43]) lies in the reconstructed OCV which is used to not only estimate the SOH but also the DMs. The OCV further is an important input for other vehicle functions, i.e., SOC estimation [8] or the fast charging strategy [52]. The studied datasets do not include a validated DM label due to the missing full OCV readouts for every SOH and the further challenging DM estimation, usually based on DVA and ICA [5]. It is possible, however, to evaluate the accuracy of the estimation by the OCV reconstruction error and the SOH estimation error. With these metrics, the ΔQ-method is further analyzed in terms of sensitivity to input data and solver settings.

4.1. Degradation mode estimation

Fig. 6 illustrates the trajectory of the estimated DMs for the cell dataset (Fig. 6(a)) and the vehicle dataset 6(b).

As expected, the DMs of the cell dataset in Fig. 6(a) generally increase with higher age. While the LAM_{PE} shows a reasonable continuous rise, LAM_{NE} and LLI increase rapidly after the first check-up at approximately 97 %. Moreover, LAM_{NE} stays constant for the consecutive two checkups. It is suspicious that the LLI decreases again. This, however, is not physically but mathematically possible if the β-parameters get closer to zero and their offset $\|\beta_{PE}| - |\beta_{NE}\|$ decreases. Hence, mathematically more lithium inventory is available for cycling again. Measured by the SOH and OCV error, the first two checkups (100 % to 97 % SOH) are estimated with high accuracy, making the DM estimation feasible. The third and fourth check-up (87 % to 84 %), however, underestimate the SOH and contain a relatively high OCV error. This makes an underestimation of the LAM_{PE} very likely. In this degraded state, LLI shows high correlation to both types of LAM due to the consumed capacity overhang. Hence, the underestimated LAM_{PE} probably leads to an underestimation of LLI and consequently the lower SOH estimate. The last check-up overestimates the SOH and shows an acceptable OCV error. The most viable option is an underestimated β_{PE} which further increases LLI.

For more samples, as visualized in Fig. 6(b) for the i3 vehicle dataset, the consistent trend of the DMs is more visible. The LAM_{NE}
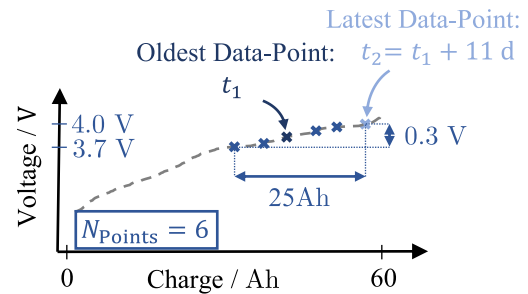

Fig. 7. Fictional sample as an example for the evaluation of applied data filters. This sample includes six data points, which were captured within a time-window of 11 days. The data points span a charge section of 25 Ah and a voltage window of 0.3 V. The minimum voltage is 3.7 V and the maximum voltage is 4.0 V.

contains the highest fluctuation, especially with the underestimation at 92 % SOH. At BOL the LLI is a result of LAM at both electrodes once the electrode capacity overhangs are consumed. Below 90 % SOH the LAM_{PE} exceeds the LAM_{NE} and LLI matches LAM_{PE} due to the oversized anode. This is reasonable due to the restricted search space of β_{PE} (Table 3) which results from the narrow voltage range of the cathode OCP measurement. This yields the fact that a decreasing α_{PE} directly influences the LLI. A strong anomaly for LAM_{PE} is visible at 82 % SOH with a decreasing slope. Analyzing Fig. 5(c) makes clear that the SOH is overestimated and hence it is reasonable that LAM_{PE} might be underestimated. Besides that, the highest SOC and OCV errors are located at 92 %, 82 % and especially 75 %. All these samples lead to anomalies in the course of the DMs. Hence, this strengthens the previous assumption of the correlation of SOH and OCV reconstruction with the DM estimation accuracy.

4.2. Sensitivity of the method to input data

In comparison to the cell dataset, the i3 vehicle dataset has relatively sparse information included. The dataset was captured from the field without focus on the ΔQ-method and hence does not include the full operational strategy between the captured points. Nevertheless, it is insightful to explore the sensitivity of the method to the initially defined settings and further to understand why the filters are set as depicted in Fig. 5(a).

To better understand the applied filters and their impact, the process of dataset filtering is explored for an example sample, as depicted in Fig. 7. The filters always refer to the full input dataset per vehicle. Hence, the Δt, max(ΔQ) and ΔV relate to several relaxed voltage points between multiple charging and driving events.

Table 5
Applied filters, their criteria and the final evaluation for the random sample in Fig. 7. For this specific example all example filters hold true and the sample could be further processed in the algorithm. The default filters do not hold true and the sample would be excluded.

Filter	Criterion	Check	Result
Example			
N_{Points}	$N \geq 5$	$6 \geq 5$	✓
Δt	$\Delta t \leq 20\,\text{d}$	$11\,\text{d} \leq 20\,\text{d}$	✓
$\max(\Delta Q)$	$\max(\Delta Q) \leq 30\,\text{Ah}$	$25\,\text{Ah} \leq 30\,\text{Ah}$	✓
ΔV	$\Delta V \leq 0.5\,\text{V}$	$0.3\,\text{V} \leq 0.5\,\text{V}$	✓
V_{start}	$V_{\text{start}} \geq 3.5\,\text{V}$	$3.7\,\text{V} \geq 3.5\,\text{V}$	✓
V_{end}	$V_{\text{end}} \leq 4.1\,\text{V}$	$4.0\,\text{V} \leq 4.1\,\text{V}$	✓
Default			
N_{Points}	$N \geq 10$	$6 \ngeq 10$	✗
Δt	$\Delta t \leq 25\,\text{d}$ *to* $40\,\text{d}$	$11\,\text{d} \leq 25\,\text{d}$	✓

Table 5 evaluates the example sample for the randomly set and the default filters. With this background knowledge, it should be straightforward to interpret the following discussion.

The possible filter variations and resulting SOH and OCV errors are visualized in Fig. 8. The default number of required points is set to 10. In contrast to the absolute variation in Fig. 8(b), the default value of the time threshold is set relative to the age (time since delivery) of the vehicle. Per default, for a BOL vehicle the last 25 days, while for an EOL vehicle up to 40 days, are used. Similar to the mileage feature, the age highly correlates with the SOH. These filters are mainly set due to the smaller number of available points for older vehicles (compare Fig. 3). Hence, increasing the time threshold for older vehicles, allows more samples with a higher number of points which cancels out the negative effect of itself. For the proposed algorithm, no filters are set regarding available voltage window, minimum and maximum voltage or maximum ΔQ. For every subfigure in Fig. 8, one variable is varied while all others are fixated to the default value. All used default settings are listed in the bottom section of Table 5. In Fig. 8 the rate of use is normalized to the number of investigated vehicles (574) and gives the number of available samples after the filtering. A small fraction ($< 10\%$) is initially unavailable due to the preset filters in Fig. 5(a) checking for feasible SOH values between 75 % to 100 %.

In practice, the algorithm already works with at least three points. As can be seen in Fig. 8(a), more sample points lead to higher accuracy. On the contrary, by requiring more points less samples fulfill these conditions. The amount of usable samples in relation to the total number of samples is referred to as rate of use. A sample size of 10 points allows high accuracy and a high rate of use. On the contrary, more points continuously lead to slightly higher OCV reconstruction errors because more points increase the complexity of the fitting process. It must be noted that the statistical significance decreases with more required points due to the smaller rate of use.

For every sample, the date of the testbench capacity measurement is not only the reference for the SOH but also to select past relaxed voltage and ΔQ pairs. In Fig. 8(b) an upwards trend in the SOH error is detectable for a longer allowed data acquisition time. This behavior is reasonable due to the continuous nature of battery aging. The OCV error slightly decreases continuously. With a looser time-threshold more points over a broader SOC range and hence more samples are available for estimation. The voltage and ΔQ information provided by additional points seems to counteract the error from increasing time windows between points. This is especially the case for MOL and EOL vehicles which have a lower frequency of recordings within specific time periods (see Fig. 3).

Fig. 8(c) shows the influence of the accumulated charge amount between relaxed voltage points. Starting with a ΔQ of 8 Ah, enough points for some samples are available to pass the prefilter. The SOH error increases over 4 % with a $\max(\Delta Q)$ of approximately 12 Ah. The error continuously decreases for higher ΔQ constraints, making clear

that with 50 Ah all possible samples are available. The OCV error follows the slope of the SOH error. This again, gives rise to the assumption of an existing correlation between the OCV reconstruction accuracy and the SOH error. The interpretation, however, must be seen in the context of the error, which fluctuates between low values of 6.6 mV to 8.0 mV.

The voltage window is analyzed in Fig. 8(d). The voltage boundaries are set according to Fig. 3. For BOL vehicles this voltage window of 0.9 V equals the SOC width from 4 % to 100 %. The correct SOC value is unknown for aged vehicles because the full and validated OCV is only known for pristine state. Hence an estimation aided by a look-up table is only possible for BOL vehicles. Due to the shifting of the OCV with degradation, huge errors are possible if the pristine OCV curves is used for a look-up table based SOC estimation. Consequently, the accuracy of the method is evaluated against varying available voltage windows instead of SOC windows. Fig. 8(d) shows the big advantage of the ΔQ-method. Accurate results are already feasible with small voltage windows, starting at 0.3 V, which equals approximately 60 % SOC for BOL vehicles if the start SOC is set to 40 %, or 45 % if the start SOC is set to 30 %, as can be seen in Fig. 5(b). The SOH error decreases with broader voltage windows and the rate of use increases. The OCV reconstruction error shows an upwards trend for broader voltage windows, giving more support to the following interpretation: It is most probable that broader voltage windows allow more uncertainty in the exact position of the relaxed voltage points which, as a result, yields a more inaccurate reconstruction.

In Figs. 8(e) and 8(f) the accuracy in dependence of the minimum and maximum voltage is depicted. With a higher minimum voltage a smaller voltage window and hence less points per sample are available. This leads to not only a lower rate of use but also a higher SOH estimation error. The dependence of the OCV reconstruction error on the minimum voltage strengthens the previously made interpretation: A smaller available voltage and charge window leads to less uncertainty and hence more precise reconstruction. In summary, a preset minimum voltage below 3.8 V is sufficient for an adequate OCV reconstruction and SOH estimation. Due to mostly present relaxation voltages at higher SOCs in all samples, the maximum voltage must be set relatively high. As can be seen in Fig. 3 most of the data is distributed at high voltage values because of many charging events. The minimum maximum voltage allowing for an adequate rate of use is 4.10 V. The error behaves mostly as expected: With a higher allowed maximum voltage more samples and points are included in the reconstruction and the SOH and OCV error decreases. Both errors inhibit a minimum for an allowed maximum voltage of 4.09 V. This, however, lacks statistical significance due to an rate of use below 20 %.

4.3. Sensitivity of the method to different solvers and settings

The solver choice and algorithm settings are evaluated. Table 6 shows the SOH error for five solvers in dependence to two varied setting: maximum evaluations or generations and function tolerance. For all solvers except *lsqnonlin()* the cost function is modified to return a scalar value.

As can be seen in Table 6, the solver choice has marginal impact on performance. The nonlinear least squares solver *lsqnonlin()* shows the best performance. The pattern search algorithm with five evaluations has the second highest accuracy but is computationally more complex [53]. The chosen maximum function tolerance of 100 assures to find the optimum without wasting computational effort and could be reduced even further. On the other side, the function tolerance does not seem to influence the accuracy at all, see Table 6. The termination tolerance on the objective function has no influence until it reaches relatively high values of almost 1×10^{-1}. Consequently, the optima in the objective functions are reached early within the optimization process, i.e., the higher function tolerance and possibly slower convergence do not hinder the algorithm to find the lowest cost function value. Starting
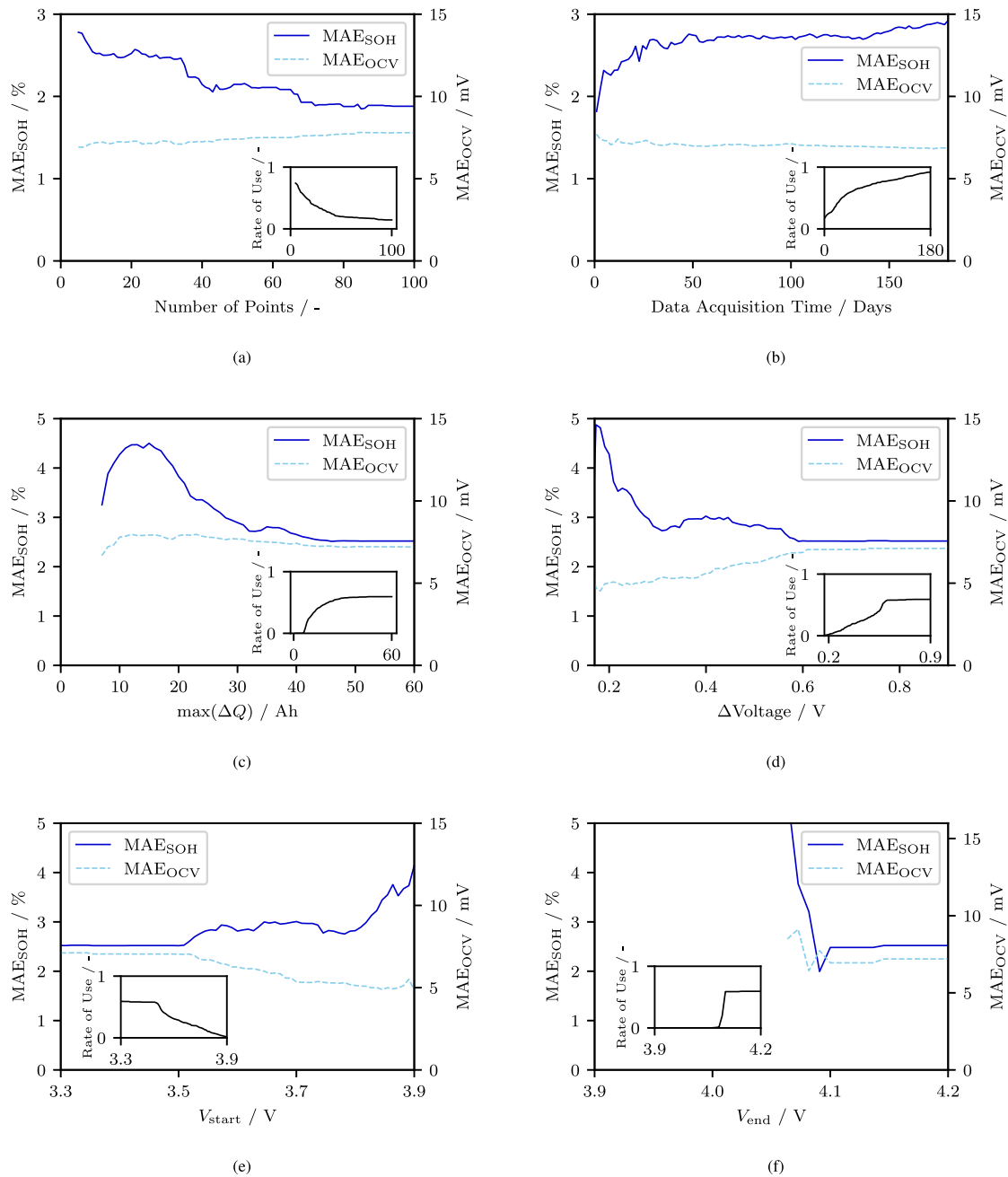
Fig. 8. Sensitivity of the ΔQ-method to specific input data filters and the resulting rate of use for the vehicle dataset. (a) Number of data points. (b) Data acquisition time horizon. (c) Maximum allowed amount of charge between two consecutive points. (d) Available voltage window in sample, where 0.9 V equals the SOC range from 4 % to 100 % for BOL batteries. (e) Minimum voltage threshold. (f) Maximum voltage threshold.

with function tolerances of 1×10^{-1} the optimization eventually stops too early and might miss the local optimum.

In summary, the designed cost function (Eq. (9)) is mathematically well-designed and robust against varying solvers and their settings. The chosen settings, as shown in Table 3, assure to find the local optimum with lowest SOH estimation and OCV reconstruction error.

4.4. Comprehensive analysis and discussion

The present study introduces a novel method for OCV reconstruction and subsequent SOH and DM estimation. The main research question at hand was whether the method is applicable to real-world data and how robust the algorithm is against varying input data and optimization settings. The application to real-world vehicle data from the BMW i3

could quantify the uncertainty of the method for the SOH estimation and demonstrate the robustness of the algorithm with respect to filter parameters and solver settings. As can be seen in Fig. 8(a), with already three relaxed voltage points and two ΔQ values, the method reaches an SOH error below 3 % and reconstructs the OCV with an average error below 10 mV. In contrast to conventional methods, the ΔQ-method does not require a fixed reference voltage for the fitting process but rather fits every voltage pair individually.

Established methods for OCV reconstruction [5,7,24–35] demand the full SOC range with relatively low C-rates to yield accurate results for DM estimation. Improved studies [37–39] established the possibility to reduce the SOC window and further increase the C-rate. Yang et al. [37] managed to use partial charging segments from 20 % to 70 % SOC with a C-rate of C/3. Similar, Chen et al. [38] reconstructed the OCV

Table 6

Sensitivity of the ΔQ-method's SOH estimation accuracy to the selected solver and specific algorithm settings, i.e., maximum function evaluations and function tolerance for termination. In the case of the genetic algorithm, the maximum function evaluations refer to the maximum number of generations and for the particle swarm it is the maximum number of iterations. The OCV fitting accuracy is almost independent (sensitivity below $\pm 1\,\text{mV}$) of the investigated settings and hence not included in this Table.

Solver	Maximum Evaluations/Generations			
	5	50	100	200
lsqnonlin	3.76 %	2.46 %	2.52 %	2.54 %
fmincon	3.34 %	2.91 %	2.88 %	2.89 %
Genetic Algorithm	2.79 %	2.96 %	2.92 %	2.86 %
Particle Swarm	2.88 %	2.88 %	2.90 %	2.90 %
Pattern Search	2.69 %	2.94 %	3.01 %	3.01 %

Solver	Function Tolerance			
	10^{-10}	10^{-8}	10^{-4}	10^{-1}
lsqnonlin	2.53 %	2.53 %	2.52 %	2.40 %
fmincon	2.88 %	2.88 %	2.88 %	2.88 %
Genetic Algorithm	2.94 %	2.88 %	2.88 %	2.91 %
Particle Swarm	2.90 %	2.90 %	2.97 %	2.96 %
Pattern Search	3.01 %	3.01 %	3.01 %	3.01 %

with partial charging segment from 40 % to 100 % SOC and a C-rate of C/3. Schmitt et al. [39] raised the applicable C-rate up to C/4 by introducing a constant overpotential offset to reconstruct the partial OCV. The offset is calculated by repetitive pulse measurements to make up for the increasing internal resistance due to aging. Nevertheless, for a C-rate of C/4 a SOC window of at least 10 % to 80 % is mandatory to create accurate capacity estimations. Accurate DM estimation is feasible for C-rates below C/15 and a maximum SOC of at least 70 %. For lower C-rates of C/30 a smaller window of 20 % to 70 % is sufficient to yield an SOH error below 2 %. The ΔQ-method, however, works without any preprocessing because the relaxed voltage points, which equal the actual OCV, are utilized in the first place. These relaxed voltage points are gathered after almost every charging or driving event, independent of the applied current and history. Figs. 8(d), 8(e) and 8(f) prove that a voltage window of at least 300 mV and a starting voltage below 3.8 V suffice to reconstruct the OCV with an error below 7 mV and estimate the SOH with an error $\leq 3\,\%$. For the pristine battery, these values correspond to a SOC window from 40 % to 100 %. For a lower starting voltage of 3.7 V the required SOC window spans from 30 % to 75 % which reduces the minimum required SOC range in comparison to known studies [37–39]. In contrast to existing methods [4,5,7,24–41], the ΔQ-method is independent of any reference charging process. It utilizes existing data from any vehicle fleet with very low sample rate and thus also low requirements with respect to bandwidth and/or storage capabilities that could be easily implemented in existing architectures. As there are no available data sources suitable for both the mechanistic model approach involving higher C-rates and partial charging segments, as well as the ΔQ-method, a comparison is performed using individual aging datasets.

The proposed method proves its suitability for given vehicle datasets, as in Fig. 5(c). With the default filters of at least 10 data points per sample, a maximum time-horizon of 25 to 40 days and the dependence on the last maximum SOH onboard estimation, a big fraction of over 59 % of the investigated vehicles with an existing testbench capacity measurement can be evaluated. The data is stored without any limitation on the operation between relaxed voltage points or temperature. It further shows in Figs. 8(b) and 8(c), that the algorithm is only slightly influenced by the time-horizon of data acquisition or the maximum allowed accumulated charge in-between voltage points, once $\max(\Delta Q) \geq 20\,\text{Ah}$. These dependencies are further canceled out by the large benefit of more sample points distributed between a large voltage window which have the biggest influence on SOH and OCV error, as Figs. 8(a), 8(d), 8(e) and 8(f) show.

Existing methods [37] usually set the constraints and boundary conditions in respect to the last evaluation. Because this method is

proposed for a vehicle fleet with at least one testbench capacity measurement during its lifetime, the boundary conditions must be set initially. The solution space, however, must be limited to reduce the risk of reaching the wrong local optimum. For this matter, the upper and lower boundaries of the α- and β-parameter are set according to the last maximum SOH onboard estimation which divides the storage into BOL, MOL and EOL, as in Table 3. Although this seems to bias the estimation towards the onboard estimation values, it must be kept in mind, that the onboard estimation is limited by the computation resources. The alignment parameter boundaries are defined loosely, to even allow out-of-bound estimations if the onboard value is completely off. Fig. 3 visualizes the strong correlation of mileage with the true SOH. It is thus possible to exchange the condition variable with either mileage or total time since production.

The total time since production is already used for setting the time-horizon filters as proposed in Fig. 5(a). Depending on this value, older vehicles use more of their history than new vehicles. While this filter hardly influences accuracy, it helps to increase the rate of use as Fig. 8(b) shows.

In comparison to the cell data results (Fig. 4(d)), the vehicle data OCV is reconstructed with similar precision over all samples (Fig. 5(c)). The OCV is only evaluated at its measured points. The reconstructed OCV is interpolated and evaluated at the respective measured charge points to calculate the OCV reconstruction error. The average number of available points for optimization, however, is 70 for the i3 dataset, assuring higher OCV reconstruction accuracy with statistical significance.

The proposed dataset is not applicable to verify the DM estimation because no full OCV measurement in aged state is available. It is only possible to evaluate the accuracy in dependence of their plausibility over SOH (Fig. 6(b)) and in terms of OCV error (Fig. 5(c)). With this mitigated criteria, the DM estimation shows reasonable trajectories.

In contrast to known methods for OCV reconstruction [4,5,7,24–41], the ΔQ-algorithm collects data from a broader time-horizon instead of relying on continuous measurements. The results in Fig. 8(b) give strong evidence that the influence of aging in data acquisition windows up to half a year is negligible. This further gives rise to the possibility to exploit this data collection scheme for time-series based algorithms, i.e., collection of several partial charging segments at a specific C-rate and subsequent reassembly.

5. Conclusion

In this work, the novel ΔQ-method was introduced and validated with real-world vehicle data gathered from more than 8 years of customer operation. The analysis showed that the method is robust to input data, solver choice and optimization settings. For the BMW i3, a minimum number of three relaxed voltage points, at least a voltage point below 3.8 V, and a minimum voltage window of 0.3 V – which combined equals a SOC window of 40 % to 100 % – were sufficient to yield SOH estimation errors below 3 %.

The algorithm is an adoption of the known mechanistic modeling approach [4] and eases the utilization for existing BEV fleets. The method does not require explicit charging segments with low C-rates but rather is applicable to relaxed voltage points and the accumulated charge between these points. No fixed reference voltage is required for the optimization process and rather every voltage pair is fitted individually during the minimization task. Analysis of the BMW i3 dataset shows that a large fraction of the studied vehicles ($\geq 59\,\%$) are enabled for application.

The proposed method shows its suitability for existing BEV fleets. Most monitoring systems collect the relaxed voltage points and track the accumulated charge. Hence, it is straightforward to use these existing datasets for OCV reconstruction if the pristine OCPs and parameter sets are known. Updated OCVs further allow calibrated SOC estimation and improved charging strategies.

The algorithm requires the latest SOH onboard estimation to constrain the solution space which is usually available for modern BEV fleets. This dependence is solvable with exchanging the criteria with aging-correlating variables, i.e., time or mileage. The method can be further enhanced by leveraging the remaining available vehicle aging data to restrict the solution space using machine learning techniques. Alternatively, combining existing methods for OCV reconstruction with the ΔQ-method can reduce uncertainty. The method's validity for DM estimation remains unconfirmed and exceeds the scope of this publication. Therefore, further evaluation of this aspect is imperative in future research endeavors. It stays an open research question whether the proposed ΔQ-method is suitable to estimate the DMs, even with narrow SOC windows of 50%. It is therefore desired to prove this assumption with an extended measurement series with full OCV measurements in the checkups, to derive the DVA and ICA which can be used to create comparable DM labels.

CRediT authorship contribution statement

Tobias Hofmann: Writing – original draft, Visualization, Validation, Software, Methodology, Investigation, Formal analysis, Conceptualization. **Jiahao Li:** Methodology, Conceptualization. **Jacob Hamar:** Writing – review & editing, Supervision. **Simon Erhard:** Writing – review & editing, Supervision. **Jan Philipp Schmidt:** Writing – review & editing, Supervision.

Declaration of competing interest

The authors declare the following financial interests/personal relationships which may be considered as potential competing interests: Tobias Hofmann reports financial support was provided by BMW Group. Jiahao Li has patent Verfahren zur Bestimmung der SOC-OCV Kennlinien und Kapazität einer Batterie mit Blendmaterialien pending to BMW Group. If there are other authors, they declare that they have no known competing financial interests or personal relationships that could have appeared to influence the work reported in this paper.

Data availability

The data that has been used is confidential.

Acknowledgments

References

[1] Z. Ma, J. Jiang, W. Shi, W. Zhang, C.C. Mi, Investigation of path dependence in commercial lithium-ion cells for pure electric bus applications: Aging mechanism identification, J. Power Sources 274 (2015) 29–40, http://dx.doi.org/10.1016/j.jpowsour.2014.10.006.

[2] L. Su, J. Zhang, J. Huang, H. Ge, Z. Li, F. Xie, B.Y. Liaw, Path dependence of lithium ion cells aging under storage conditions, J. Power Sources 315 (2016) 35–46, http://dx.doi.org/10.1016/j.jpowsour.2016.03.043.

[3] T. Raj, A.A. Wang, C.W. Monroe, D.A. Howey, Investigation of path-dependent degradation in lithium-ion batteries, Batteries Supercaps 3 (2020) 1377, http://dx.doi.org/10.1002/batt.202000160.

[4] M. Dubarry, C. Truchot, B.Y. Liaw, Synthesize battery degradation modes via a diagnostic and prognostic model, J. Power Sources 219 (2012) 204–216, http://dx.doi.org/10.1016/j.jpowsour.2012.07.016.

[5] C.R. Birkl, M.R. Roberts, E. McTurk, P.G. Bruce, D.A. Howey, Degradation diagnostics for lithium ion cells, J. Power Sources 341 (2017) 373–386, http://dx.doi.org/10.1016/j.jpowsour.2016.12.011.

[6] P.M. Attia, A. Bills, F.B. Planella, P. Dechent, G.d. Reis, M. Dubarry, P. Gasper, R. Gilchrist, S. Greenbank, D. Howey, O. Liu, E. Khoo, Y. Preger, A. Soni, S. Sripad, A.G. Stefanopoulou, V. Sulzer, Review—Knees in lithium-ion battery aging trajectories, J. Electrochem. Soc. 169 (2022) 060517, http://dx.doi.org/10.1149/1945-7111/ac6d13.

[7] J.P. Schmidt, H.Y. Tran, J. Richter, E. Ivers-Tiffée, M. Wohlfahrt-Mehrens, Analysis and prediction of the open circuit potential of lithium-ion cells, J. Power Sources 239 (2013) 696–704, http://dx.doi.org/10.1016/j.jpowsour.2012.11.101.

[8] G.L. Plett, Extended Kalman filtering for battery management systems of LiPB-based HEV battery packs: Part 1. Background, J. Power Sources 134 (2) (2004) 252–261, http://dx.doi.org/10.1016/j.jpowsour.2004.02.031.

[9] J. Newman, N.P. Balsara, Electrochemical Systems, 4th Edition, John Wiley % Sons, ISBN: 978-1-119-51459-6, 2021.

[10] M. Doyle, T.F. Fuller, J. Newman, Modeling of galvanostatic charge and discharge of the lithium/polymer/insertion cell, J. Electrochem. Soc. 140 (1993) 1526, http://dx.doi.org/10.1149/1.2221597.

[11] T.F. Fuller, M. Doyle, J. Newman, Simulation and optimization of the dual lithium ion insertion cell, J. Electrochem. Soc. 141 (1994) 1, http://dx.doi.org/10.1149/1.2054684.

[12] A. Allam, S. Onori, Online capacity estimation for lithium-ion battery cells via an electrochemical model-based adaptive interconnected observer, IEEE Trans. Control Syst. Technol. 29 (2021) 1636–1651, http://dx.doi.org/10.1109/TCST.2020.3017566.

[13] X. Zhao, Y. Bi, S.-Y. Choe, S.-Y. Kim, An integrated reduced order model considering degradation effects for LiFePO4/graphite cells, Electrochim. Acta 280 (2018) 41–54, http://dx.doi.org/10.1016/j.electacta.2018.05.091.

[14] P. Gambhire, K.S. Hariharan, A. Khandelwal, S.M. Kolake, T. Yeo, S. Doo, A physics based reduced order aging model for lithium-ion cells with phase change, J. Power Sources 270 (2014) 281–291, http://dx.doi.org/10.1016/j.jpowsour.2014.07.127.

[15] Y. Gao, K. Liu, C. Zhu, X. Zhang, D. Zhang, Co-estimation of state-of-charge and state-of- health for lithium-ion batteries using an enhanced electrochemical model, IEEE Trans. Ind. Electron. 69 (2022) 2684–2696, http://dx.doi.org/10.1109/TIE.2021.3066946.

[16] X. Sui, S. He, S.B. Vilsen, J. Meng, R. Teodorescu, D.-I. Stroe, A review of non-probabilistic machine learning-based state of health estimation techniques for lithium-ion battery, Appl. Energy 300 (2021) 117346, http://dx.doi.org/10.1016/j.apenergy.2021.117346.

[17] K. Luo, X. Chen, H. Zheng, Z. Shi, A review of deep learning approach to predicting the state of health and state of charge of lithium-ion batteries, J. Energy Chem. 74 (2022) 159–173, http://dx.doi.org/10.1016/j.jechem.2022.06.049.

[18] Q. Gong, P. Wang, Z. Cheng, A data-driven model framework based on deep learning for estimating the states of lithium-ion batteries, J. Electrochem. Soc. 169 (2022) 030532, http://dx.doi.org/10.1149/1945-7111/ac5bac.

[19] W. Li, N. Sengupta, P. Dechent, D. Howey, A. Annaswamy, D.U. Sauer, Online capacity estimation of lithium-ion batteries with deep long short-term memory networks, J. Power Sources 482 (2021) 228863, http://dx.doi.org/10.1016/j.jpowsour.2020.228863.

[20] Y. Choi, S. Ryu, K. Park, H. Kim, Machine learning-based lithium-ion battery capacity estimation exploiting multi-channel charging profiles, IEEE Access 7 (2019) 75143–75152, http://dx.doi.org/10.1109/ACCESS.2019.2920932.

[21] K. Luo, H. Zheng, Z. Shi, A simple feature extraction method for estimating the whole life cycle state of health of lithium-ion batteries using transformer-based neural network, J. Power Sources 576 (2023) 233139, http://dx.doi.org/10.1016/j.jpowsour.2023.233139.

[22] J. Yang, B. Xia, W. Huang, Y. Fu, C. Mi, Online state-of-health estimation for lithium-ion batteries using constant-voltage charging current analysis, Appl. Energy 212 (2018) 1589–1600, http://dx.doi.org/10.1016/j.apenergy.2018.01.010.

[23] J. Cannarella, C.B. Arnold, State of health and charge measurements in lithium-ion batteries using mechanical stress, J. Power Sources 269 (2014) 7–14, http://dx.doi.org/10.1016/j.jpowsour.2014.07.003.

[24] M. Dubarry, M. Berecibar, A. Devie, D. Anseán, N. Omar, I. Villarreal, State of health battery estimator enabling degradation diagnosis: Model and algorithm description, J. Power Sources 360 (2017) 59–69, http://dx.doi.org/10.1016/j.jpowsour.2017.05.121.

[25] Z. Ma, Z. Wang, R. Xiong, J. Jiang, A mechanism identification model based state-of-health diagnosis of lithium-ion batteries for energy storage applications, J. Clean. Prod. 193 (2018) 379–390, http://dx.doi.org/10.1016/j.jclepro.2018.05.074.

[26] C. Pastor-Fernández, T.F. Yu, W.D. Widanage, J. Marco, Critical review of non-invasive diagnosis techniques for quantification of degradation modes in lithium-ion batteries, Renew. Sustain. Energy Rev. 109 (2019) 138–159, http://dx.doi.org/10.1016/j.rser.2019.03.060.

[27] J.P. Fath, D. Dragicevic, L. Bittel, A. Nuhic, J. Sieg, S. Hahn, L. Alsheimer, B. Spier, T. Wetzel, Quantification of aging mechanisms and inhomogeneity in cycled lithium-ion cells by differential voltage analysis, J. Energy Storage 25 (2019) 100813, http://dx.doi.org/10.1016/j.est.2019.100813.

[28] K.M. Mbeya, N. Damay, G. Friedrich, C. Forgez, M. Juston, Off-line method to determine the electrode balancing of li-ion batteries, Math. Comput. Simulation 183 (2021) 34–47, http://dx.doi.org/10.1016/j.matcom.2020.02.013.

[29] D. Anseán, G. Baure, M. González, I. Cameán, A.B. García, M. Dubarry, Mechanistic investigation of silicon-graphite/LiNi0.8Mn0.1Co0.1O2 commercial cells for non-intrusive diagnosis and prognosis, J. Power Sources 459 (2020) 227882, http://dx.doi.org/10.1016/j.jpowsour.2020.227882.

[30] S. Lee, J.B. Siegel, A.G. Stefanopoulou, J.-W. Lee, T.-K. Lee, Electrode state of health estimation for lithium ion batteries considering half-cell potential change due to aging, J. Electrochem. Soc. 167 (2020) 090531, http://dx.doi.org/10.1149/1945-7111/ab8c83.

[31] B. Pan, D. Dong, J. Wang, J. Nie, S. Liu, Y. Cao, Y. Jiang, Aging mechanism diagnosis of lithium ion battery by open circuit voltage analysis, Electrochim. Acta 362 (2020) 137101, http://dx.doi.org/10.1016/j.electacta.2020.137101.

[32] M. Dubarry, D. Beck, Perspective on mechanistic modeling of li-ion batteries, Accounts Mater. Res. 3 (2022) 843–853, http://dx.doi.org/10.1021/accountsmr.2c00082.

[33] I. Bin-Mat-Arishad, B. Wimarshana, A. Fly, Influence of voltage profile and fitting technique on the accuracy of lithium-ion battery degradation identification through the voltage profile model, J. Energy Storage 70 (2023) 107884, http://dx.doi.org/10.1016/j.est.2023.107884.

[34] M. Dubarry, V. Agrawal, M. Hüske, M. Kuipers, Accurate LLI and LAMPE estimation using the mechanistic modeling approach with layered oxides, J. Electrochem. Soc. 170 (2023) 070503, http://dx.doi.org/10.1149/1945-7111/ace21c.

[35] J. Schmitt, M. Schindler, A. Oberbauer, A. Jossen, Determination of degradation modes of lithium-ion batteries considering aging-induced changes in the half-cell open-circuit potential curve of silicon–graphite, J. Power Sources 532 (2022) 231296, http://dx.doi.org/10.1016/j.jpowsour.2022.231296.

[36] S. Schindler, G. Baure, M.A. Danzer, M. Dubarry, Kinetics accommodation in li-ion mechanistic modeling, J. Power Sources 440 (2019) 227117, http://dx.doi.org/10.1016/j.jpowsour.2019.227117.

[37] S. Yang, C. Zhang, J. Jiang, W. Zhang, Y. Gao, L. Zhang, A voltage reconstruction model based on partial charging curve for state-of-health estimation of lithium-ion batteries, J. Energy Storage 35 (2021) 102271, http://dx.doi.org/10.1016/j.est.2021.102271.

[38] J. Chen, M.N. Marlow, Q. Jiang, B. Wu, Peak-tracking method to quantify degradation modes in lithium-ion batteries via differential voltage and incremental capacity, J. Energy Storage 45 (2022) 103669, http://dx.doi.org/10.1016/j.est.2021.103669.

[39] J. Schmitt, M. Rehm, A. Karger, A. Jossen, Capacity and degradation mode estimation for lithium-ion batteries based on partial charging curves at different current rates, J. Energy Storage 59 (2023) 106517, http://dx.doi.org/10.1016/j.est.2022.106517.

[40] D. Lu, M.S. Trimboli, G. Fan, R. Zhang, G.L. Plett, Implementation of a physics-based model for half-cell open-circuit potential and full-cell open-circuit voltage estimates: Part II. Processing full-cell data, J. Electrochem. Soc. 168 (2021) 070533, http://dx.doi.org/10.1149/1945-7111/ac11a5.

[41] Z. Cui, N. Cui, C. Li, J. Lu, C. Zhang, Online identification and reconstruction of open-circuit voltage for capacity and electrode aging estimation of lithium-ion batteries, IEEE Trans. Ind. Electron. 70 (2023) (2023) 4716–4726, http://dx.doi.org/10.1109/TIE.2022.3187596.

[42] M. Dubarry, D. Beck, Big data training data for artificial intelligence-based li-ion diagnosis and prognosis, J. Power Sources 479 (2020) 228806, http://dx.doi.org/10.1016/j.jpowsour.2020.228806.

[43] M. Dubarry, D. Beck, Analysis of synthetic voltage vs. Capacity datasets for big data li-ion diagnosis and prognosis, Energies 14 (2021) 2371, http://dx.doi.org/10.3390/en14092371.

[44] N. Costa, L. Sánchez, D. Anseán, M. Dubarry, Li-ion battery degradation modes diagnosis via convolutional neural networks, J. Energy Storage 55 (Part C) (2022) 105558, http://dx.doi.org/10.1016/j.est.2022.105558.

[45] J. Tian, R. Xiong, W. Shen, F. Sun, Electrode ageing estimation and open circuit voltage reconstruction for lithium ion batteries, Energy Storage Mater. 37 (2021) 283–295, http://dx.doi.org/10.1016/j.ensm.2021.02.018.

[46] X. Liu, S. Li, J. Tian, Z. Wei, P. Wang, Health estimation of lithium-ion batteries with voltage reconstruction and fusion model, Energy 282 (2023) 128216, http://dx.doi.org/10.1016/j.energy.2023.128216.

[47] W. Li, J. Chen, K. Quade, D. Luder, J. Gong, D.U. Sauer, Battery degradation diagnosis with field data, impedance-based modeling and artificial intelligence, Energy Storage Mater. 53 (2022) 391–403, http://dx.doi.org/10.1016/j.ensm.2022.08.021.

[48] F. Roeder, S. Ramasubramanian, A review and perspective on path dependency in batteries, Energy Technol. 10 (2022) 2200627, http://dx.doi.org/10.1002/ente.202200627.

[49] M. Dubarry, G. Baure, D. Anseán, Perspective on state-of-health determination in lithium-ion batteries, J. Electrochem. Energy Convers. Storage 17 (4) (2020) 044701, http://dx.doi.org/10.1115/1.4045008.

[50] T. Hofmann, J. Hamar, M. Rogge, C. Zoerr, S. Erhard, J.P. Schmidt, Physics-informed neural networks for state of health estimation in lithium-ion batteries, J. Electrochem. Soc. 170 (2023) 090524, http://dx.doi.org/10.1149/1945-7111/acf0ef.

[51] Matlab, Lsqnonlin Documentation, The MathWorks, Inc., 2023, https://de.mathworks.com/help/optim/ug/lsqnonlin.html. (accessed 19 July 2023).

[52] C. Zoerr, J.J. Sturm, S. Solchenbach, S.V. Erhard, A. Latz, Electrochemical polarization-based fast charging of lithium-ion batteries in embedded systems, J. Energy Storage 72 A (2023) 108234, http://dx.doi.org/10.1016/j.est.2023.108234.

[53] S. Jiang, B. Peng, O. Weinstein, The complexity of dynamic least-squares regression, 2023, http://dx.doi.org/10.48550/arXiv.2201.00228, arXiv preprint.